



Validation of structural brain connectivity networks

The impact of scanning parameters

Ambrosen, Karen S.; Eskildsen, Simon F.; Hinne, Max; Krug, Kristine; Lundell, Henrik; Schmidt, Mikkel N.; van Gerven, Marcel A.J.; Mørup, Morten; Dyrby, Tim B.

Published in:
NeuroImage

Link to article, DOI:
[10.1016/j.neuroimage.2019.116207](https://doi.org/10.1016/j.neuroimage.2019.116207)

Publication date:
2020

Document Version
Publisher's PDF, also known as Version of record

[Link back to DTU Orbit](#)

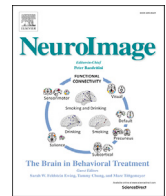
Citation (APA):
Ambrosen, K. S., Eskildsen, S. F., Hinne, M., Krug, K., Lundell, H., Schmidt, M. N., van Gerven, M. A. J., Mørup, M., & Dyrby, T. B. (2020). Validation of structural brain connectivity networks: The impact of scanning parameters. *NeuroImage*, 204, Article 116207. <https://doi.org/10.1016/j.neuroimage.2019.116207>

General rights

Copyright and moral rights for the publications made accessible in the public portal are retained by the authors and/or other copyright owners and it is a condition of accessing publications that users recognise and abide by the legal requirements associated with these rights.

- Users may download and print one copy of any publication from the public portal for the purpose of private study or research.
- You may not further distribute the material or use it for any profit-making activity or commercial gain
- You may freely distribute the URL identifying the publication in the public portal

If you believe that this document breaches copyright please contact us providing details, and we will remove access to the work immediately and investigate your claim.



Validation of structural brain connectivity networks: The impact of scanning parameters



Karen S. Ambrosen^{a,b}, Simon F. Eskildsen^c, Max Hinne^d, Kristine Krug^{e,f,g}, Henrik Lundell^b, Mikkel N. Schmidt^a, Marcel A.J. van Gerven^d, Morten Mørup^a, Tim B. Dyrby^{b,a,*}

^a Department of Applied Mathematics and Computer Science, Technical University of Denmark, Kgs. Lyngby, Denmark

^b Danish Research Centre for Magnetic Resonance, Center for Functional and Diagnostic Imaging and Research, Copenhagen University Hospital Hvidovre, Hvidovre, Denmark

^c Center of Functionally Integrative Neuroscience (CFIN), Department of Clinical Medicine, Aarhus University, Aarhus, Denmark

^d Donders Institute for Brain, Cognition and Behaviour, Radboud University, Nijmegen, the Netherlands

^e Department of Physiology, Anatomy and Genetics, University of Oxford, Oxford, UK

^f Institute of Biology, Otto-von-Guericke-Universität Magdeburg, Magdeburg, Germany

^g Leibniz-Institute for Neurobiology, Magdeburg, Germany

ABSTRACT

Evaluation of the structural connectivity (SC) of the brain based on tractography has mainly focused on the choice of diffusion model, tractography algorithm, and their respective parameter settings. Here, we systematically validate SC derived from a *post mortem* monkey brain, while varying key acquisition parameters such as the b-value, gradient angular resolution and image resolution. As gold standard we use the connectivity matrix obtained invasively with histological tracers by Markov et al. (2014). As performance metric, we use cross entropy as a measure that enables comparison of the relative tracer labeled neuron counts to the streamline counts from tractography. We find that high angular resolution and high signal-to-noise ratio are important to estimate SC, and that SC derived from low image resolution (1.0^3 mm^3) are in better agreement with the tracer network, than those derived from high image resolution (0.5^3 mm^3) or at an even lower image resolution (2.0^3 mm^3). In contradiction, sensitivity and specificity analyses suggest that if the angular resolution is sufficient, the balanced compromise in which sensitivity and specificity are identical remains 60–64% regardless of the other scanning parameters. Interestingly, the tracer graph is assumed to be the gold standard but by thresholding, the balanced compromise increases to 70–75%. Hence, by using performance metrics based on binarized tracer graphs, one risks losing important information, changing the performance of SC graphs derived by tractography and their dependence of different scanning parameters.

1. Introduction

Tractography based on diffusion magnetic resonance imaging (dMRI) is a unique non-invasive tool for studying both specific brain connections (i.e. tracts), as well as their contribution to the structural brain network (i.e. structural connectivity (SC)), the so-called connectome (Hagmann, 2005; Sporns et al., 2005) and to the brain's structural organisation (Craddock et al., 2013; Le Bihan and Johansen-Berg, 2012; Toga et al., 2006; Van Essen et al., 2014). Analyzing whole brain SC using graph theoretic measures has been useful for classification of healthy and diseased subjects (Iturria-Medina, 2013). When using tractography to study specific tracts, diffusion tensor imaging (DTI) (Basser et al., 1994; Pierpaoli et al., 1996) or other local microstructural estimates can be related to clinical scores (Giorgio et al., 2010), brain maturation and ageing (Bennett et al., 2010; Lebel et al., 2008). Furthermore,

tractography enables parcellation of the cortex (Ambrosen et al., 2014; Anwander et al., 2007; Baldassano et al., 2015; Fan et al., 2016; Parisot et al., 2016) or subcortical structures based on SC (Behrens et al., 2003a; Wiegell et al., 2003).

The estimation of the brain's structural organisation consists of a comprehensive data processing pipeline (Jones et al., 2013; Jones and Cercignani, 2010; Qi et al., 2015). All the methodological choices and parameter settings potentially affect the estimation of the brain connections and have an impact on the resultant SC. These include acquisition settings of dMRI (e.g b-value, angular resolution, image resolution and the resulting signal-to-noise ratio (SNR)), correction of acquisition-related artefacts (motion, susceptibility, etc.), local fiber reconstruction from dMRI (model selection), and tractography (algorithm selection, number of streamlines, curvature threshold, step length, definition of seeding strategy and target regions, etc.), as well as choices

* Corresponding author. Danish Research Centre for Magnetic Resonance, section 714, Copenhagen University Hospital Hvidovre, Kettegaard Alle 30, 4623, Hvidovre, Denmark.

E-mail address: timd@drctr.dk (T.B. Dyrby).

<https://doi.org/10.1016/j.neuroimage.2019.116207>

Received 25 April 2019; Received in revised form 20 August 2019; Accepted 17 September 2019

Available online 17 September 2019

1053-8119/© 2019 Elsevier Inc. All rights reserved.

in the post-tractography stage (streamline count thresholding, normalization, etc.). Tractography only indirectly relates to physiological properties of the axonal connections, such as conduction velocity, delays and directionality. It does not map individual axon projections as with neuronal tracers (Dyrby et al., 2018). Instead, brain connections are based on streamlines that are drawn in a stepwise manner by following the orientation of voxelwise anisotropic profiles expressing local fiber architecture captured by dMRI (cell and axon density and directions). Several studies have shown that this indirect, but non-invasive fiber tracking of the brain network is challenged by the generation of multiple false-positive connections (de Reus and van den Heuvel, 2013; Dyrby et al., 2007; Knösche et al., 2015; Maier-Hein et al., 2017; Thomas et al., 2014). The ISMRM 2015 tractography challenge based on a human brain phantom with ground truth-connections revealed how dependent the tractography results are on the individual processing steps. Also, it showed how the bottlenecks, i.e. spatially narrow regions through which more connections are projected, are the main source of false positives (Maier-Hein et al., 2017). Thus, validation of the derived SC is of great importance (Fornito et al., 2013). Nevertheless, a vast amount of tractography studies demonstrate its potential for studying the structural organisation of both the healthy (Gong et al., 2009; Robinson et al., 2010; Wen et al., 2011) and the diseased brain (Jahanshad et al., 2015; Lo et al., 2010; Shu et al., 2011; Skudlarski et al., 2010; Zalesky et al., 2011). Although all methodological choices and parameter settings in the tractography affect the derived SC, another important factor is how the underlying axonal information is represented in the dMRI dataset given the selected scanning parameters, and how it influences the SC analysis. (Fornito et al., 2013).

Until now, validation studies of SC have focused on the tractography methods and their cross-comparison, both for extracting specific tracts, their exact projections and for networks (Bastiani et al., 2012; Caiafa and Pestilli, 2017; Dyrby et al., 2007; Thomas et al., 2014; Villalon-Reina et al., 2016), as well as the influence of tractography-specific parameters, such as FA threshold (Azadbakht et al., 2015; Bastiani et al., 2012; Dauguet et al., 2007), curvature threshold (Azadbakht et al., 2015; Bastiani et al., 2012; Dauguet et al., 2007), integration step length (Dauguet et al., 2007), and probabilistic thresholding (Bastiani et al., 2012). Previous studies have tested how different parameters affect the estimated connectome. This has been done either by investigating how different graph measures, such as graph density, shortest paths, etc., are affected (Bastiani et al., 2012), or by studying the variations between the SC based upon by tractography (Gigandet et al., 2013; Jones, 2004; Zalesky et al., 2012, 2010; Zhan et al., 2012) and in the individual estimated WM tracts (Berman et al., 2013; Gigandet et al., 2013; Vos et al., 2016). Alternatively, tractography has been validated by comparison to histological tracer studies, either by comparing specific tracts (Azadbakht et al., 2015) or by comparing the SC with a network obtained using invasive tracers (Azadbakht et al., 2015; Calabrese et al., 2015; Donahue et al., 2016; van den Heuvel et al., 2015). Invasive tracers can be used to verify both the connectivity (i.e. whether or not two regions are connected) and the projection (i.e. the route and shape of the tract). In validation studies, the quality of the dMRI data is often commended to be a possible factor to improve the resultant SC. However, studies investigating the impact of key data acquisition parameters, i.e., angular resolution, b-value and spatial image resolution, on the derived connectome are still limited. For example, Schilling et al. (2017) find that the estimated number of crossing fibers increase with increased spatial resolution and recommend to focus on SNR, angular resolution and b-value. Zhan et al. (2012) show that the final connectome is affected by spatial and angular resolutions, but do not validate the estimated connectomes.

Here, we provide an extensive validation of the impact of such key data acquisition parameters using an *ex vivo* acquisition setup in the macaque brain. Estimation of SC in *post mortem* brains has been shown to be a good model for human brain SC, as long as the b-value is adjusted to the lower diffusivity *ex vivo* (D'Arceuil et al., 2007; Dyrby et al., 2011; Sun et al., 2005). Specifically, we quantify how spatial image resolution,

angular resolution and b-value affect the final connectome. Furthermore, the effects of streamline count threshold, seeding strategy, number of acquisitions versus SNR and the integration step-length in the tractography algorithm are quantified. The generated connectomes across different combinations of parameters are validated by comparison to the state-of-the-art 91×29 tract tracing graph of the macaque brain generated using retrograde tracers (Markov et al. (2014)). In the comparison, cross entropy is used as a performance metric measure of correspondence in addition to sensitivity and specificity, where the tracer graph is assumed to be the ground truth.

2. Materials and methods

2.1. Animals

One *post mortem* brain from a male Rhesus macaque (M105) was scanned using dMRI. The animal was 4 years and 10 months old and weighed 10.1 kg at the time of perfusion. M105 was perfused and fixed at Oxford University (see Ahmed et al. (2012) for the perfusion protocol). When the brain was removed from the skull (*post mortem*), two approx. 10 mm deep incisions were made in the brain tissue of the occipital lobe in the left hemisphere, which cut the white matter tract to the occipital region, see Fig. S1. Since the tract was cut *post mortem*, the integrity of the axons around the disruption was not affected. The incision can be seen on high image resolution MRI. Despite the incision, the left hemisphere was included in the analyses as an additional validation of our setup, expecting it to be in less agreement with the tracer graph than the fully intact hemisphere. At lower image resolutions the increased partial volume effect (PVE) will be used to illustrate how PVE and image resolution can affect measurements of SC. All animal procedures were carried out in accordance with Home Office (UK) Regulations and European Union guidelines (EU directive 86/609/EEC; EU Directive, 2010/63/EU).

2.2. MRI acquisition

Imaging of the *ex vivo* monkey brain was performed on an experimental 4.7 T Agilent scanner with a quadrature volume RF coil and a maximum gradient strength of 600 mT/m. Free fixative was washed out to increase T2, using phosphate buffer following the preparation stages according to the setup in (Dyrby et al., 2011). The brain was placed in a sealed plastic bag with minimal phosphate buffered saline (PBS) surrounding the brain tissue and stabilized to room temperature before scanning. Using a mechanically stable setup, the brain was placed in the middle of the volume coil. To ensure constant temperature while scanning, a constant flow of room temperature air around the brain was used, and the temperature was measured at the end of the magnet. To ensure removal of any short-term mechanic and thermal instabilities, a diffusion weighted pre-scan with a duration of 18 h was acquired (Dyrby et al., 2011). The scanning protocol used a pulsed gradient spin-echo sequence with single-line readout. Whole-brain coverage and high image resolution with isotropic 0.5^3 mm^3 voxels was obtained with a matrix size of 128×256 , field-of-view: $64 \times 128 \text{ mm}^2$, 91 slices. Three shells with different b-values were acquired: $b = [1477, 4102, 8040] \text{ s/mm}^2$ by varying the gradient strength, $G = [150, 250, 350] \text{ mT/m}$ and keeping constant gradient length $\delta = 8 \text{ ms}$, gradient separation $\Delta = 17 \text{ ms}$ as well as the echo time $TE = 30 \text{ ms}$. In terms of signal attenuation, the b-values for *ex vivo* can roughly be translated to *in vivo* as ~ 800 , ~ 1000 and $\sim 3000 \text{ s/mm}^2$. The relationship is determined from estimations of the WM diffusion coefficient *in vivo* versus *ex vivo* (Dyrby et al., 2018; Dyrby et al., 2011; D'Arceuil et al., 2007; Sun et al., 2005). The number of $b = 0 \text{ s/mm}^2$ i.e. b_0 per shell are 3. The repetition time was $TR = [8000, 7900, 8600] \text{ ms}$. Each b-value was acquired using a shell that included in total 180 directions, generated by using electrostatic dipole repulsion (Jones, 2004). The 180 shell was designed to include a subset of 20 and 60 uniformly distributed directions; Firstly, 20 uniformly distributed directions were generated. These were held fixed

and 40 additional directions were generated such that in total 60 directions were approximately uniformly distributed. The same procedure was applied when generating in total 180 directions by keeping the optimally distributed 60 directions fixed. The protocol was repeated 3 times for the 20 directions protocol and 2 times for the 60 and 180 directions protocols. The total scan time was about 15.3 days. The data sets including raw dMRI and processed surfaces can be downloaded from Danish Research Centre for Magnetic Resonance (DRCMR) (<http://drcmr.dk/map-datasets>) and from the White Matter Microscopy Database (<https://osf.io/yp4qq/>).

2.3. Data pre-processing

Visual quality inspection of the *ex vivo* dMRI dataset revealed no need for any post-processing such as distortion correction or registration. A brain mask was generated by averaging all diffusion-weighted images (i.e. excluding b_0), followed by thresholding, binarizing, and subsequently manual editing using FSLview. A mean b_0 was generated from all the b_0 's and used for the generation of surfaces defining target and seed regions in the tractography. See Fig. 1 for the outline of the data processing.

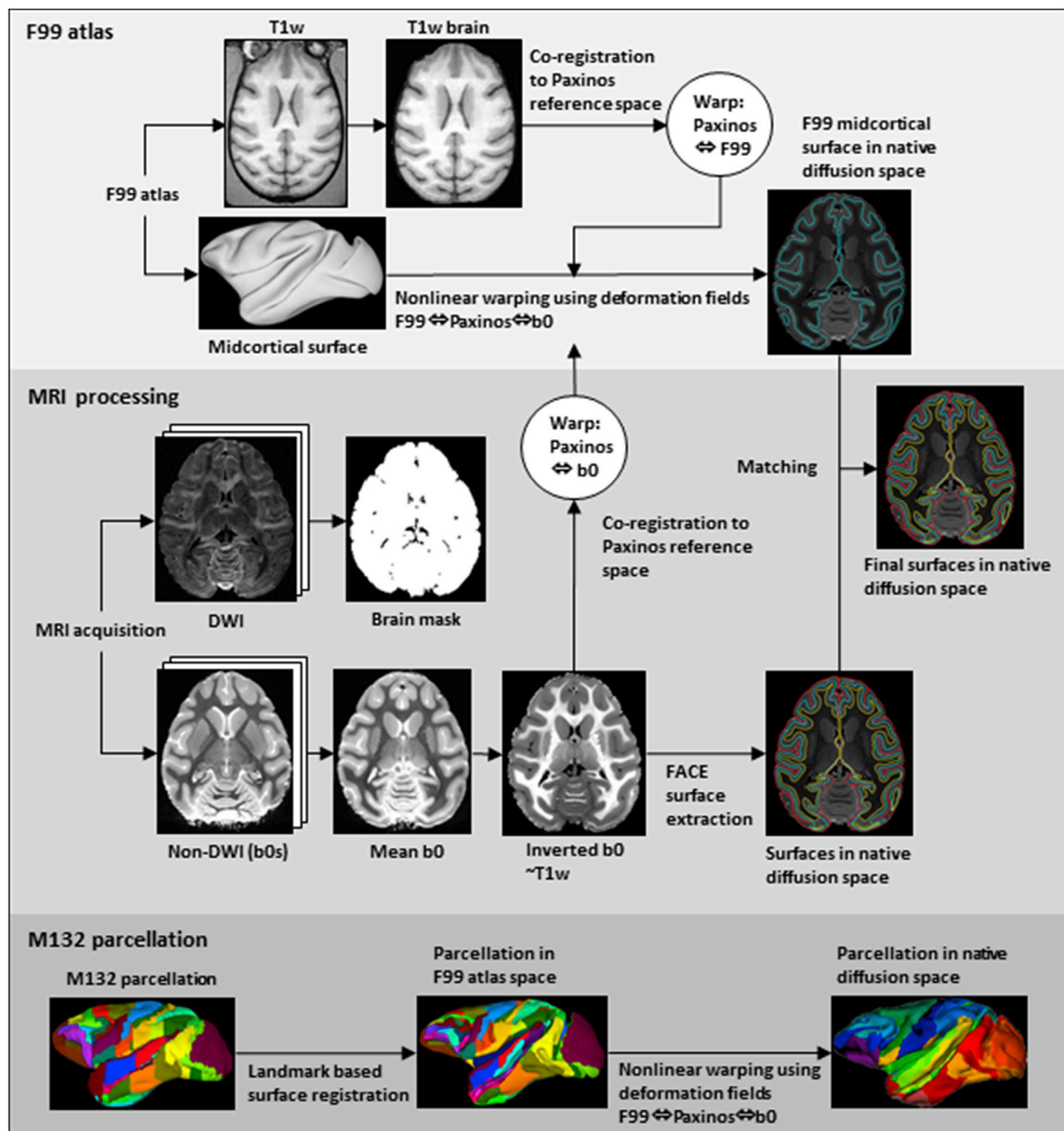


Fig. 1. Outline of the data processing. The top area with the beige background shows the processing of the F99 atlas: brain extraction of the T1-weighted image and co-registration to Paxinos reference space. Furthermore, nonlinear warping of the midcortical surface in F99 space to Paxinos reference space. The middle area with light grey background shows the MRI processing. A brain mask is derived from the DWIs and is used in the tractography. The non-DWIs (b_0 s) are averaged and inverted to imitate a T1-weighted image and linear and non-linear registered to the Paxinos reference space. WM, midcortical and GM surfaces are extracted from the inverted b_0 -image in Paxinos reference space. Lastly, the F99 midcortical surface in native diffusion space are matched to the three surfaces in native diffusion space to yield the final surfaces in native diffusion space. The bottom area with dark grey background shows the processing of the M132 parcellation. First, it is registered to the F99 atlas space and secondly warped to native diffusion space.

2.3.1. Generation of different image resolutions

In Dyrby et al. (2014) we acquired different image resolutions and experienced that the image grid is not guaranteed to be the same across image resolutions. This introduces a risk for different PVE's especially at the interface between tracts that can influence tractography comparisons. Therefore, low image resolution dMRI datasets with 1.0^3 and 2.0^3 mm³ isotropic image resolution were generated as post-processing by linearly down-sampling the acquired high-resolution image datasets with a factor of 8 and 64 using the FSL tool (Jenkinson et al., 2012; Smith et al., 2004; Woolrich et al., 2009). The sampling of a 2ⁿ factor ensures that new voxels were centred on the grid of original voxels, emulating the exact acquisition of that spatial image resolution. We use a linear interpolation which does not introduce blurring, as typically seen for higher order interpolation methods (Dyrby et al., 2015). The image resolutions of the *ex vivo* monkey investigated are then 0.5^3 , 1.0^3 and 2.0^3 mm³. Assuming a volume ratio of 13 times between the human and macaque brain, the corresponding image resolutions in the human brain will roughly be $\sim 1.2^3$, $\sim 2.3^3$ and $\sim 4.7^3$ mm³.

2.4. Cortical parcellations and surfaces

2.4.1. Pre-processing

The intensities of mean b0 were inverted to better match intensities of a T1w image. Subsequently, the intensity-swapped image was denoised (Coupe et al., 2008) and bias-field corrected (Sled et al., 1998). The F99 atlas in vivo T1-weighted image was skull-stripped, using the FSL brain extraction tool and the eyes were manually removed. Both images were then linearly and nonlinearly warped to a reference space defined by the Paxinos atlas, using a combination of FLIRT, MINC tools, and Advanced Normalization Tools (ANTs) (Avants et al., 2008). The surface extraction process on the b0 image was performed in linear Paxinos reference space.

2.4.2. Surface extraction

Three surfaces were generated to be used in tractography, i.e. the WM-GM, GM-CSF and the middle cortical layer surfaces. The pre-processed mean b0 in Paxinos reference space was used to generate cortical surfaces by applying Fast Accurate Cortex Extraction (FACE) (2006; Eskildsen et al., 2005; Eskildsen and Ostergaard, 2007). Probability maps for white matter (WM), grey matter (GM), and cerebrospinal fluid (CSF) were calculated using a fuzzy clustering algorithm. The WM probability map was thresholded, amended with a mask of deep GM structures warped from the template, and topology corrected (Chen and Wagenknecht, 2006). An initial surface was generated by applying marching cubes on the resulting WM component (Lorensen and Cline, 1987). This initial WM surface was iteratively fitted to the cortical WM-GM interface. The resulting surface was subsequently fitted to the GM-CSF interface by inflating the surface as described in (Eskildsen and Ostergaard, 2006). A surface estimating the middle cortical layer was subsequently generated from the WM-GM surface and GM-CSF surface. The final WM-GM surface in native diffusion space contained 118,671 vertices in the left hemisphere and 121,818 vertices in the right hemispheres.

2.4.3. Cortical parcellation

As cortical parcellation, we used the M132 parcellation containing 91 cortical regions mapped to the left hemisphere of an individual macaque (case M132). The M132 macaque was registered to the F99 atlas, using landmark-based surface registration (Van Essen, 2002; Van Essen and Dierker, 2007).

The F99 atlas mid-cortical surface was nonlinearly warped to Paxinos reference space, using the previously calculated deformation field from the F99 atlas (Van Essen, 2002) to the b0 image in Paxinos reference space. The mean b0 mid-cortical surface was then matched to the F99 atlas surface, using a feature-driven surface registration algorithm (Eskildsen and Ostergaard, 2008).

The M132 parcellation was mapped to the b0 image WM-GM surface

via the b0 mid-cortical surface and the inherent correspondence obtained from the FACE process. Coherent labels were ensured by morphologically removing any label-wise “salt-and-pepper noise” in the mapped parcellation. Since no vertices on the native WM surface were assigned to the piriform region, this region was excluded and only the 90×29 tracer graph was used in the analysis.

2.5. Tractography

The fiber orientation distributions were estimated using FSL's bedpostX algorithm allowing up to three crossing fibers per voxel (Jbabdi et al., 2013; Behrens et al., 2007; Jbabdi et al., 2013). Probabilistic tractography was performed in native space, using the algorithm implemented in FSL's probtrackx2 (Behrens et al., 2007; 2003b). In the tractography, a step length of $\frac{1}{4}$ voxel size, i.e. 0.125 mm and 0.25 mm for the spatial resolution of 0.5^3 mm³ and 1.0^3 mm³ respectively, was used as is common practice (Jbabdi et al., 2013; Thomas et al., 2014) along with a curvature constraint of 80°. The maximum number of steps was adjusted based on the step length to ensure that the maximum streamline length was well above the size of the brain. Two different seeding strategies were applied, WM seeding and GM seeding. In WM seeding, the thresholded WM probability map was used as seed mask. All voxels were seeded with 2000 streamlines and only those streamlines that intersected the WM-GM surface at two locations were kept. For further details on the choice of the number of streamlines, see Fig. S2 and (Ambrosen et al., 2014). In GM seeding, 5000 streamlines were initiated in each vertex of the WM-GM surface and streamlines that reached another vertex of the WM-GM surface were kept. For both seed strategies, an exclusion mask including subcortical structures was created from the template, and the ventricles generated by segmenting CSF from the mean b0 image using FSL's FAST algorithm (Zhang et al., 2001) in conjunction with manual editing. Streamlines transversing the exclusion mask were excluded. Finally, streamlines transversing the GM-CSF surface were terminated.

The retrograde tracer data was only available for intrahemispheric connections, and hence the tractography was performed for the two hemispheres separately.

2.6. SC graphs

2.6.1. The SC graph from tractography

Both WM and GM seeding strategies resulted in two SC matrices, **A**, one for each hemisphere. The size of the SC matrices was determined by the number of vertices on the WM-GM surface, yielding a $118,671 \times 118,671$ matrix for the left hemisphere and a $121,818 \times 121,818$ matrix for the right hemisphere. The SC matrices obtained using WM seeding were symmetric due to the bidirectional approach, whereas the SC matrices obtained from GM seeding were made symmetric by taking the arithmetic mean of the streamline counts, i.e. $\frac{A_{ij} + A_{ji}}{2}$.

The SC graphs were subsampled to the size of the tracer graph by adding the number of streamlines connecting the vertices within the regions defined by the M132 parcellation. To investigate the effect of thresholding the tractography, different streamline count thresholds were applied to the SC graphs. The thresholds reflect percentiles of the non-zero elements in the SC graphs. Thresholds of 0–80% with increment of 20% were applied to the full resolution tractography graph, corresponding to setting the top 20–100% strongest connection weights to 1 and all other connections to 0. Because the streamline count thresholds were applied before the subsampling, we obtained binary full resolution graphs, which subsequently were subsampled to the size of the tracer graph. This was done by summarizing the number of binary connections between vertices belonging to each region of the tracer graph. The weights of the tractography graph in the resolution of the tracer graph is thus the number of vertices connecting each pair of regions defined by

the M132 parcellation and hence not the streamline counts from the tractography.

When running tractography, different combinations of parameters were investigated: Three b-values (1477, 4102 and 8040 s/mm²), three directional protocols (20, 60 and 180 directions) with a number of repeated excitations (NEX) (3, 2, and 2), three image resolutions (0.5³ mm³, 1.0³ mm³, 2.0³ mm³), two seeding strategies (WM and GM seeding), two hemispheres, six streamline count thresholds, two step lengths, as well as different a number of acquisition repetitions with different SNR. This resulted in 3456 SC graphs to be validated against the tracer graph.

2.6.2. The retrograde tract tracing graph

As a ground truth SC graph, we used a tracer connectivity dataset collected in macaque monkeys by Markov et al. (2014), quantifying the intrahemispheric interareal connectivity of the macaque cerebral cortex, using retrograde tracer injections. Retrograde tracers were injected into 29 regions, and labeled neurons were counted in 91 regions, generating a 91 × 29 weighted and directed connectivity graph. The volume of the injections varied across injection areas (0.1–0.6 μL) (Markov et al., 2011). Brain regions were defined by a reference atlas containing 91 cortical regions mapped to the left hemisphere of an individual macaque (M132). Although tracers were injected in both hemispheres, Markov et al. mapped all source and target (injection) sites to the left hemisphere. The weights in the graph are the extrinsic fraction of labeled neurons (FLNe). The FLNe value of an area was estimated by the number of labeled neurons in that area relative to the total number of labeled neurons excluding the labeled neurons intrinsic to the injected area (Markov et al., 2011; Markov et al., 2014). That is,

$$FLNe_j(i) = \frac{|i|}{|k| - |j|},$$

where $|i|$ is the number of labeled neurons in the source area (from where the projection originates), $|k|$ is the total number of labeled neurons in the brain, and $|j|$ is the number of labeled neurons in the target area (injection area, where the retrograde tracer is taken up by nerve endings). As the FLNe values are normalized by the total number of labeled neurons in the brain (excluding the labeled neurons in the target area), the number of labeled neurons from each injection area sum to one and can thus be treated as a probability distribution. The FLNe values in the tracer graph are assumed ground truth in our validation of SC graphs. The tracer data have been obtained from <http://core-nets.org>.

2.7. Performance metrics for validation

Three performance metrics were used to compare the estimated SC graphs from tractography with the FLNe values of the tracer graph considered as ground truth probabilistic connectivity estimates; cross entropy, sensitivity, and specificity. Cross entropy takes the distribution of FLNe values into account and is thereby used to assess the correspondence in weights between the tracer graph and the SC graphs. Cross entropy is related to the Kullback-Leibler metric previously employed in Pestilli et al. (2014). Sensitivity and specificity as proposed in Donahue et al. (2016) threshold the FLNe values at zero corresponding to presence or absence of connections, and is used to assess the overlap in binary topology. Hence, the relative strengths of the tracer connections are not considered in these latter two validation measures. All the considered validation metrics were investigated for different streamline thresholds and seeding strategies.

2.7.1. Robust estimation of cross entropy

To evaluate the quality of the extracted SC graphs, we calculated the cross entropy (Kullback and Leibler, 1951; Shannon, 1948) between the tract tracing graph (Markov et al., 2014) based on the FLNe values, denoted as $\vec{\theta}_j^{gt}$ for a given target region j , and the corresponding SC

graphs. Cross entropy is an information theoretic measure of the average information needed to encode data from a “true” probability distribution (FLNe tracer data) using a “surrogate” distribution (SC data). In other words, cross entropy measures how close the estimated distribution is to the true distribution. Cross entropy was calculated column-wise between the SC graph subsampled to the size of the tracer graph and the tracer graph. If the dMRI graph was not symmetric by generation, it was made symmetric by taking the arithmetic mean before subsampling to the size of the tracer graph. The cross entropy (H) was given by

$$H(\vec{\theta}_j^{gt}, \vec{\theta}_j) = H(\vec{\theta}_j^{gt}) + D_{KL}(\vec{\theta}_j^{gt} \parallel \vec{\theta}_j) = -\sum_i \vec{\theta}_j^{gt} \log(\vec{\theta}_{ij}), \quad (1)$$

where $H(\vec{\theta}_j^{gt})$ was the entropy of $\vec{\theta}_j^{gt}$, $D_{KL}(\vec{\theta}_j^{gt} \parallel \vec{\theta}_j)$ was the Kullback-Leibler divergence from the distribution of relative SC probabilities derived from the SC graph, $\vec{\theta}_j$ to the distribution of relative tracer connectivity probabilities $\vec{\theta}_j^{gt}$. The j index was the target region (columns in the tracer graph), and the i index was the source region (rows in the tracer graph). As can be observed from equation (1), the expression for cross entropy is asymmetric in the sense that interchanging what is considered the “true” and “surrogate” distribution in general changes the cross entropy value. Choosing FLNe obtained from tracer data as the “true” distribution makes it possible to compare different SC graphs’ ability to encode the tracer FLNe which would not be possible if interchanging the role of the tracer and tractography data, whereby the cross entropy would exhibit differing off-sets depending on the complexity (i.e. entropy) of the distribution of relative SC probabilities.

In order to quantify the cross entropy, the distribution of relative SC probabilities $\vec{\theta}_j$, which was unknown, needed to be estimated from the SC graph. As cross entropy was not defined in regions where $\vec{\theta}_{ij}$ was zero (i.e., $\log(0) = -\infty$), this distribution had to be robustly estimated. We therefore inferred $\vec{\theta}_j$, using Bayesian inference (Hinne et al., 2015). The (prior) probability of a streamline reaching one of the cortical regions in the M132 parcellation was modelled by a Dirichlet distribution with the parameter $\vec{\alpha}_j$ defined by the relative size of the cortical regions \mathbf{V} , where V_i refers to the size of source region i . The SC between a target region and all source regions $\vec{\alpha}_j$ (where a_{ij} was the number of connections between source region i and target region j) was modelled by a multinomial distribution, where each of the total of N_j connections between the sources and target j had the probability distribution $\vec{\theta}_j$. The generative model was thus defined by

$$\vec{\theta}_j \sim \text{Dir}(\kappa_j \vec{\alpha}_j), \quad \vec{\alpha}_j = \frac{V_i}{\sum_{i \neq j} V_i} \quad (2)$$

$$\vec{\alpha}_j \sim \text{Mult}(\vec{\theta}_j, N_j), \quad (3)$$

Where κ_j was a scaling factor specifying the confidence of the prior.

We learned κ_j by exploiting that the Dirichlet distribution was conjugate to the Multinomial distribution such that $\vec{\theta}_j$ could be analytically marginalized:

$$p(\vec{\alpha}_j | \kappa_j \vec{\alpha}_j) = \int p(\vec{\alpha}_j | \vec{\theta}_j) p(\vec{\theta}_j | \kappa_j \vec{\alpha}_j) d\vec{\theta}_j = \frac{N_j!}{\prod_{i \neq j} a_{ij}!} \frac{B(\vec{\alpha}_j + \kappa_j \vec{\alpha}_j)}{B(\kappa_j \vec{\alpha}_j)} \quad (4)$$

where $B(\cdot)$ is the multivariate beta function.

The value of κ_j was then found empirically by optimizing the log of this marginalized distribution, i.e. $\log(p(\vec{\alpha}_j | \kappa_j \vec{\alpha}_j))$. In the optimization¹

¹ Optimization was performed using the minimum bound optimization *fminbnd* in Matlab v. 8.5.1 (The MathWorks Inc., Natick, MA, 2000).

κ_j was constrained to the interval $\left[0, \sum_{i \neq j} \alpha_{ij}\right]$ such that κ_j always was non-negative and the prior never could have more influence than the diffusion data.

Using Bayes' theorem, the posterior distribution of $\vec{\theta}_j$ was then given by the Dirichlet distribution

$$p(\vec{\theta}_j | \vec{\alpha}_j, \kappa_j, \vec{\alpha}_j) = \frac{p(\vec{\alpha}_j | \vec{\theta}_j) p(\vec{\theta}_j | \kappa_j \vec{\alpha}_j)}{\int p(\vec{\alpha}_j | \vec{\theta}_j) p(\vec{\theta}_j | \kappa_j \vec{\alpha}_j) d\vec{\theta}_j} = \text{Dir}(\vec{\alpha}_j + \kappa_j \vec{\alpha}_j) \quad (5)$$

From this distribution, we used the expected value of $\vec{\theta}_j$ given by

$$\left\langle \vec{\theta}_j \right\rangle = w_j \vec{r}_j + (1 - w_j) \vec{\alpha}_j \quad (6)$$

as an estimate of the relative SC probabilities, where

$$\alpha_{ij} = \frac{V_i}{\sum_{i \neq j} V_i}, \quad r_{ij} = \frac{a_{ij}}{\sum_{i \neq j} a_{ij}}, \quad w_j = \frac{\sum_{i \neq j} \alpha_{ij}}{\sum_{i \neq j} (a_{ij}) + \kappa_j}, \quad (1 - w_j) = \frac{\kappa_j}{\sum_{i \neq j} (a_{ij}) + \kappa_j}$$

2.7.2. ANOVA analysis

A three-factor repeated measures ANOVA with Bonferroni correction and Greenhouse-Geisser correction for sphericity was performed in SPSS 19 to investigate the effect of varying the b-value, image resolution and angular resolution, as well as their interactions. The ANOVA was based on the quantified cross entropy values and repeated for all target regions (columns of the graphs).

2.7.3. Sensitivity and specificity

Sensitivity was defined by the number of (binary, i.e. non-weighted) links co-occurring in the tracer and tractography graphs divided by the total number of connections in the tracer graph. Specificity was defined by the number of absent connections co-occurring in the tracer and tractography graphs divided by the total number of absent connections in the tracer graph. The full resolution diffusion graphs were thresholded at different percentiles of non-zero elements in the diffusion graphs. The binary counts in the full resolution graphs were summed according to the cortical regions, corresponding to the size of the tracer graph (sub-sampling step).

The subsampled graphs were binarized, such that only information about whether two regions were connected or not were kept. Subsequently, sensitivity and specificity were calculated between the thresholded and subsampled binary diffusion graph and the binary tracer graph thresholded by $FLNe > 0$. In the optimal case both sensitivity and specificity are 100%, but that is, unfortunately, rarely the case. Herein, we define the balanced compromise between sensitivity and specificity as the point where they are equal. Additionally, receiver operator characteristic (ROC) curves were created. To create the ROC curves, the subsampled diffusion graphs were thresholded at different levels, from 0 to 100%, and the true positive rates (sensitivity) vs false positive rates (1-specificity) were plotted. When calculating the ROC curves, the thresholds were applied to the subsampled graphs, e.g. the SC graphs with the same size as the tracer graph. The thresholds were applied to the subsampled graph instead of to the full resolution SC graphs, as done in the cross entropy analyses, due to computational limitations.

3. Results

Ex vivo diffusion-weighted imaging of a Rhesus macaque brain was obtained under different scanning parameters. Fig. 2 shows a color-coded fractional anisotropy (FA) map for different combinations of angular and image resolutions. Independent of the number of directions, the overall gross anatomical structures that appear at high image resolution are also

visible in the lower image resolution. However, at low image resolution, anatomical features suffer from severe partial volume effects (PVE), e.g. major WM structures such as corpus callosum (yellow arrows) are only few voxels thick in the low image resolution (left) compared to the high-resolution images (middle and right). Some fine anatomical details visible at the eight times higher image resolution are missing in the FA map at low image resolution. Generally, larger tracts appear discontinuous at low image resolution and are often only one voxel thick as seen for the corpus callosum (yellow arrows). Low angular resolution (right) makes the FA map appear noisier compared to the FA map with higher angular resolution at the same image resolution (middle).

3.1. Network similarity measured with cross entropy

The cross entropy between the SC graphs based on tractography and the tracer graph when using WM seeding and without thresholding of the full resolution SC graphs (i.e. using streamlines counts) is reported in Fig. 3. Generally, more directions consistently improve cross entropy (i.e. cross entropy decreases) between the graphs (3-factor repeated measures ANOVA, $F(1.041, 29.144) = 11.443$, $p = 0.002$), suggesting that angular resolution is essential for the agreement between the SC graph and the tracer graph. The interaction between the spatial (white vs. grey background in Fig. 3) and angular resolution is significant (3-factor repeated measures ANOVA, $F(1.164, 32.601) = 15.412$, $p < 0.001$). Furthermore, the main effect of the b-value is not significant (3-factor repeated measures ANOVA, $F(1.483, 41.520) = 2.132$, $p = 0.143$), but the interaction between the b-value and image resolution is (3-factor repeated measures ANOVA, $F(1.640, 45.923) = 8.457$, $p = 0.001$). These results suggest that increasing angular resolution and b-value is more beneficial for high-resolution than for low-resolution data.

Interestingly, lower image resolution improves the cross entropy in all parameter configurations (3-factor repeated measures ANOVA, $F(1, 28) = 10.278$, $p = 0.003$). Even for the combination of highest angular resolution (180 directions) and highest b-value ($b = 8040$ s/mm²), the low image resolution-based networks outperform those generated from the high image resolution. Results on different tractography thresholds are shown in SI, Fig. S3. When performing GM seeding the same dependency on the acquisition parameters - image resolution, angular resolution and b-value - is observed (results not shown).

3.2. Interaction between SNR, image resolution and angular resolution

We then asked the question if the improved SC performance at the lower image resolution compared to the higher resolution could be explained by a higher SNR due to its larger voxel size. Rician noise, with a standard deviation of 95, was added to the low image resolution images to match the SNR of the high resolution (Gudbjartsson and Patz, 1995). Fig. 4 shows the comparison of graphs obtained using high image resolution (0.5³ mm³) and the low image resolution (1.0³ mm³) with added noise, and clearly, the agreement with the tracer graph decreases. However, the graphs derived from the low image resolution images with noise added are still in better agreement with the tracer graph. Independent of b-value and SNR matched image resolutions, the graphs from the 20 directional protocol perform worse than graphs derived from higher angular resolution data. Interestingly, low angular resolution have a greater negative impact on the high image resolution graphs (white background) than on the low image resolution graphs (grey background).

Since the total number of acquisitions, i.e. directions impact the SNR hence cross entropy, we investigated the effect of having an identical number of total acquisitions versus angular resolution. Fig. 5 shows, that independent of image resolution it is always better to use more acquisitions to improve SNR. Additionally, more unique directions (e.g. 60 directions) compared to repetitions of fewer directions (e.g. 3×20 directions) is the best choice. Similar results are obtained for GM seeding.

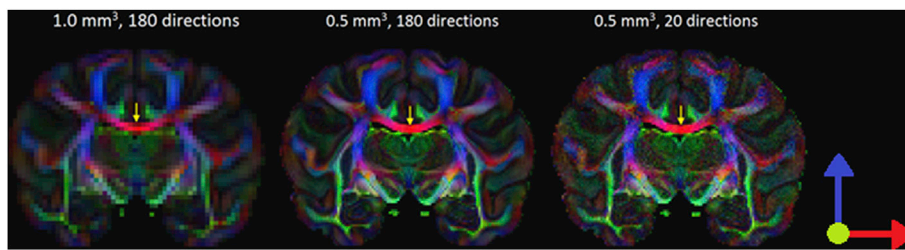


Fig. 2. Colour-coded fractional anisotropy (FA) map (red: left-right, green: anterior-posterior, blue: superior-inferior). The images are acquired with a b-value of 4102 s/mm². Left: low image resolution (1.0³ mm³) and 180 directions, middle: high image resolution (0.5³ mm³) and 180 directions and right: high image resolution (0.5³ mm³) and 20 directions. Yellow arrows indicate midpoint of the corpus callosum.

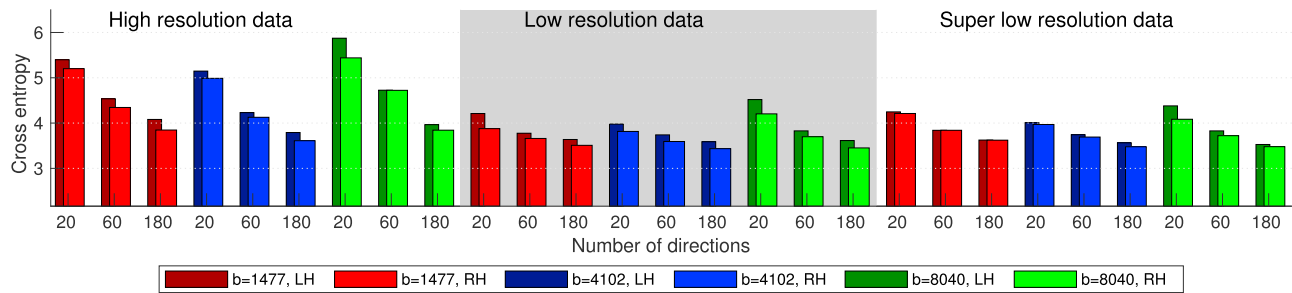


Fig. 3. Cross entropy between tracer graph and diffusion graphs generated using different acquisition parameters and WM seeding. A low cross entropy represents a high correspondence. The different colours indicate the three different b-values (red: 1477 s/mm², blue: 4102 s/mm², green: 8040 s/mm²), with darker nuances indicating data from the left hemisphere, whereas bright colours indicate data from the right (fully intact) hemisphere. The background colour indicates the image resolution, where high resolution is 0.5³ mm³ (left white background), low resolution is 1.0³ mm³ (grey background) and super low resolution is 2.0³ mm³ (right white background). The minimum value on the y-axis (2.17) indicates the entropy of the tracer graph, hence the height of the bars is the KL divergence.

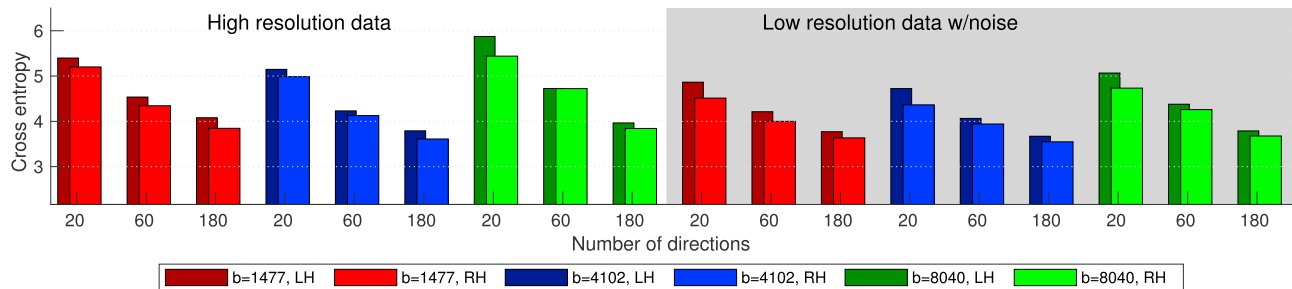


Fig. 4. Comparison of high image resolution data (0.5³ mm³) with low SNR (18.22 ± 1.07) and low image resolution data (1.0³ mm³) with added noise to simulate the SNR of the high image resolution data (SNR = 18.31 ± 0.91). The different colours show different b-values (red: 1477 s/mm², blue: 4102 s/mm², green: 8040 s/mm²). Dark colours show the results from the left hemisphere and bright colours show the results from the right (intact) hemisphere. WM seeding is performed.

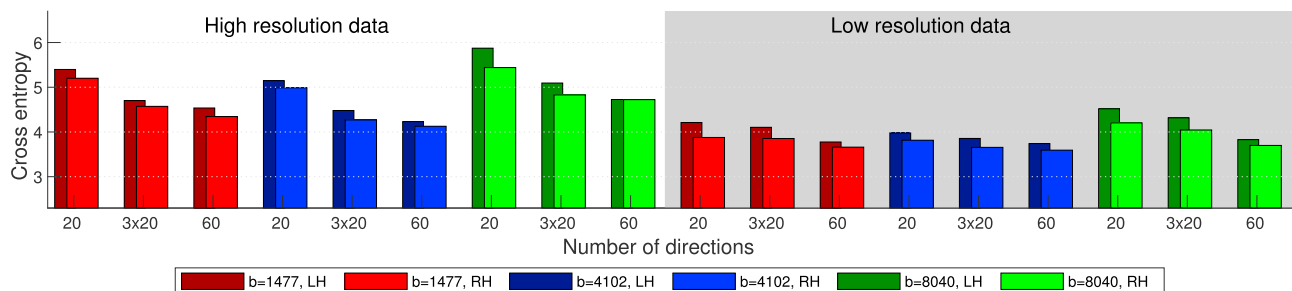


Fig. 5. Comparison of graphs derived from data acquired with various number of acquisitions and/or number of excitations (NEX) for a shell. Results for high and low image resolution data, i.e. 0.5³ and 1.0³ mm³ respectively. The different colours show different b-values (red: 1477 s/mm², blue: 4102 s/mm², green: 8040 s/mm²). Dark colours show the results from the left hemisphere and bright colours show the results from the right (intact) hemisphere. WM seeding is performed.

3.3. Interaction between image resolution and the step size in the tractography

Finally, we explored if the better correspondence with tracer data using the low-compared to the high image resolution (although a matched SNR) can be explained by fewer steps in the tractography needed to connect cortical regions. The step size was changed from $\frac{1}{4}$ of the voxel size, i.e. 0.125 mm and 0.25 mm, to be fixed independent of voxel size. The results are shown in Fig. 6. Large (0.25 mm) step length, independent of the other parameters (image resolution, angular resolution, and b-value), increases the agreement with the tracer graph. The results also show that the cross-entropy derived from the high image resolution is higher than (or are at least on par with) the cross-entropy derived from the low image resolution with added noise.

3.4. Partial volume effects (PVE) impact SC

Due to the incisions, i.e. small cuts, made to some occipital WM connections when removing the brain from the skull in the left hemisphere (Fig. S1), the right hemisphere generally shows a higher agreement with the tracer graph (Figs. 2–5, left hemisphere narrower bars with darker color nuances). However, lowering the image resolution to an even coarser image resolution, i.e. 2.0^3 mm^3 , results in the left hemisphere starting to align with the (fully intact) right hemisphere due to severe PVE that reduces the isotropic contribution at the incision (Fig. 3).

3.5. Sensitivity and specificity

Fig. 7 shows the sensitivity and specificity for all combinations of parameters, using WM seeding in the right (intact) hemisphere. Fig. 7 illustrates that for all combinations of parameters the balanced compromise between sensitivity and specificity is around 60–64%, except for the combination of high b-value ($b = 8040 \text{ s/mm}^2$), low angular resolution (20 directions), and high image resolution (0.5^3 mm^3) where it is not defined (Fig. 7 top left). Interestingly, if the angular resolution is high enough, the sensitivity and specificity curves become independent of the other scan parameters (image resolution and b-value), but dependent on the streamline count threshold. Results for the left hemisphere show the same trend (results not shown). Similarly, we see that the Pearson linear correlation and the Spearman rank correlation between the FLNe values in the tracer graph and the counts in the SC graphs based on tractography are very dependent on the streamline count threshold (SI, Figs. S4 and S5). For some thresholds, the performance of the graphs are independent of the scanning parameters (e.g. spearman rank correlation without thresholding; Fig. S5, top row). Also, when varying the threshold the best performing combination of parameters change. This is, in contradiction to the results, obtained using cross entropy, where the ranking of the graphs stayed constant when applying different streamline count thresholds.

The ROC curves shown in Fig. 8 (A, E) support the findings in Fig. 7

that the sensitivity and specificity characteristics are optimal around 60–64% independent of acquisition parameters, i.e., image resolution, the b-value, but also the angular resolution. We investigated if the difference between the sensitivity/specificity results and the cross entropy results can be explained by binarizing the tracer graph. Increasing the threshold of the tracer graph, i.e. $\text{FLNe} > [0, 25, 50, 75]\%$ of the FLNe counts, resulted in link densities of [67, 50, 33, 17]%. The sensitivity and specificity increase for increasing threshold of the tracer graph, independent of scan parameters (Fig. 8). By increasing the threshold of the tracer graph, the low image resolution (E-H) compared with the higher (A-D) improves the false positive rate (FPR), i.e. [38, 35, 30, 26]% versus [39, 37, 34, 28]%. By calculating the AUC scores, we find that the low image resolution performs slightly better than the high image resolution, corresponding to our findings using cross entropy. The contrast between the image resolutions is, however, greater when using cross entropy. ROC curves for the left hemisphere show the same trend, but the AUC scores are in general lower (results not shown).

3.6. Seeding strategies: GM versus WM seeding

SC graphs are based upon the use of both WM seeding and GM seeding, and the analyses are repeated for both seeding strategies. The effect of seeding strategy has minimal influence on the cross entropy results (results not shown). Similarly, the points where the sensitivity and specificity curves are crossing (i.e. optimal balance) remains constant, independent of seeding strategy, but the streamline count threshold changes (results not shown).

4. Discussion

We have systematically quantified the extent to which SC graphs derived from tractography are dependent on the acquisition parameters; b-value, image resolution, and angular resolution. However, the results were largely dependent on the performance metric used and whether it used thresholding for binarization or not i.e. ROC or cross-entropy similarity measures. We find that networks generated from low, but not too low, image resolution datasets better agree with ground truth than graphs derived from a dataset with eight times higher image resolution which have a correspondingly lower SNR. Interestingly, this result holds for any combination of b-values, angular resolution, and seeding strategy, although low angular resolution exhibits the worst performance. Even though finer anatomical details are available at higher image resolutions (Dyrby et al., 2014; Schilling et al., 2017; Sotiropoulos et al., 2013), the better performance of the low image resolution graphs suggests that the SC is driven by gross brain structures i.e. bigger sized tracts. These bigger tracts are expected to be present at the lower image resolution data, which also benefits of higher SNR where SC analysis performs better. Thus, our results suggest that an improvement in the image resolution is not guaranteed to improve SC analysis if it does not change the geometrical representation of brain connections and ensures

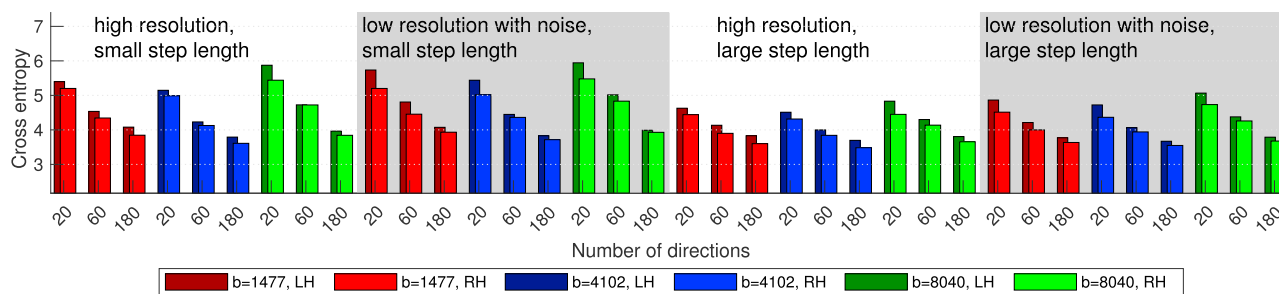


Fig. 6. Comparison of graphs derived from data with similar SNR and using the same step length in the tractography. The different colours show different b-values (red: 1477 s/mm^2 , blue: 4102 s/mm^2 , green: 8040 s/mm^2). Dark colours show the results from the left hemisphere and bright colours show the results from the right (intact) hemisphere. WM seeding is performed.

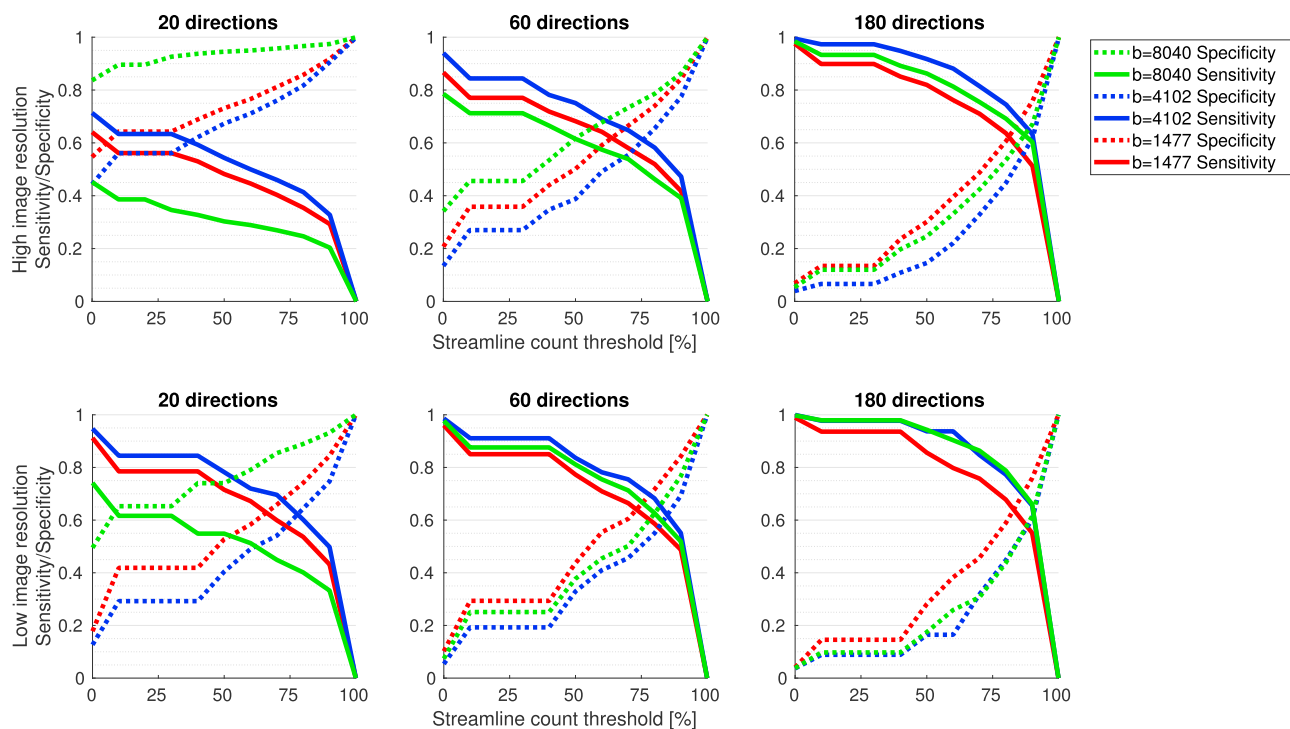


Fig. 7. Sensitivity and specificity versus streamline count threshold in percentage of maximum count value for different combinations of b-value (different colours), angular resolution (different columns), and image resolutions (different rows). Results are obtained using WM seeding and shown for the right hemisphere only. The intersections between the sensitivity and specificity curves indicate a balanced compromise between sensitivity and specificity. The balanced compromise between sensitivity and specificity is maintained at 60–64% for all combinations of parameters, except for the combination of high image resolution (0.5^3 mm^3), high b-value (8040 s/mm^2) and low angular resolution (20 directions).

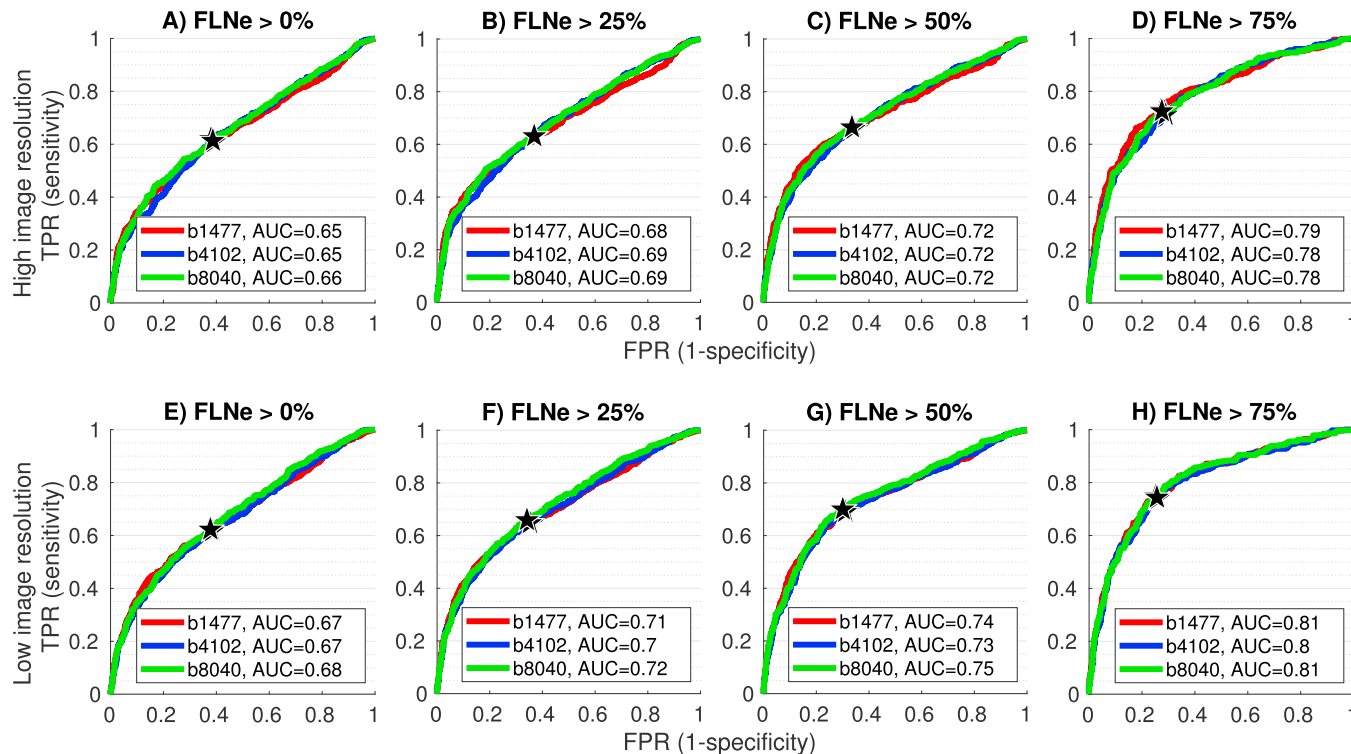


Fig. 8. ROC curves for the right (intact) hemisphere derived from high resolution (0.5^3 mm^3) images (A–D) and low resolution (1.0^3 mm^3) images (E–H), using WM seeding. The columns show the ROC curves when different thresholds of FLNe counts are used to binarize the tracer graph. The thresholds are: (A,E) $\text{FLNe} > 0\%$ as traditionally used, (B,F) $\text{FLNe} > 25\%$, (C,G) $\text{FLNe} > 50\%$ and (D,H) $\text{FLNe} > 75\%$. The angular resolution is 180 directions and the colours show different b-values (red: 1477, blue: 4102, green: 8040). The stars indicate the balanced compromise between sensitivity and specificity, and the higher the threshold, the better the performance, especially for the low image resolution. TPR: True positive rate, FPR: False positive rate.

improved SNR (see discussion in Dyrby et al., 2014). It should be emphasized that SC analysis presented here is different from tract “segmentation” analysis. SC analysis focus on the connectivity e.g. streamline counts at source and target regions, without much focus on the trajectory, whereas tract segmentation focus on correct delineation of the shape and trajectory of a tract and is sensitive to image resolution (Maier-Hein et al., 2017; Vos et al., 2016). For broad use of a dMRI dataset, it should always be acquired with the highest possible image resolution in relation to SNR and angular resolution. Down-sampling methods can be applied as a post-processing step (as done here) if a lower image resolution optimizes the SC analysis results.

4.1. The impact of angular resolution, SNR and b-value

We find that more angular directions are always to be preferred, independent of the other parameters. This agrees with the results by (Tournier et al., 2012), who recommends using as high an angular resolution as scan time allows. However, the question may rise whether the improved performance of the higher angular resolution data simply is due to a higher SNR because it has more acquisitions than the low angular resolution data (Zhan et al., 2010). We show that this is not the case. Too low an angular resolution cannot be compensated by increased SNR. To make the graphs comparable, we compared an equal number of acquisitions, i.e. the average of three repeats of 20 directions versus one with 60 directions (Fig. 5). For high image resolution, increased SNR obtained by averaging multiple repetitions increases the agreement with the tracer graph, but does not outperform the graphs with similar SNR generated using a higher angular resolution. However, for low image resolution data, where partial volumes of multiple fiber populations are more prominent, high angular resolution significantly improves the result.

Graphs based on high b-value datasets benefit more from high angular resolution than the graphs acquired using low b-values. A possible explanation is that the estimated orientation distributions get more peaked when increasing the b-value and therefore more directions are needed to describe the distributions (Dyrby et al., 2011; Frank, 2002, 2001; Xie et al., 2015). By increasing the b-value, signal contributions from the extracellular space contribute decrease, resulting in broadening of the fiber orientation profile and thereby suppressing uncertainties in the streamline tracking. However, it should be noted that the interaction effect between b-value and angular resolution was not found to be significant.

An explanation why angular resolution is a key parameter over image resolution and SNR may be found in how streamlines are drawn stepwise in the current tractography methods. Theoretically, the low-resolution images contain the same anatomical (directional) anisotropic diffusivity information within a voxel as the high-resolution images, except that the fiber orientation information is merged into fewer voxels. Therefore, a multi-fiber reconstruction method can, within a voxel, extract the same (multiple) major fiber directions in the low resolution images as are distributed over several voxels in the higher resolution images. However, fiber reconstruction methods all constrain the reconstructed fiber directions to the geometrical center of a voxel. This means that although similar multi-fiber directions can be reconstructed at the lower image resolution with high SNR, some spatial information will be lost if the underlying anatomy, i.e. axonal bundles, at the higher image resolution has a different projection through the geometrical center of the low image resolution voxel.

In the generation of connectomes, we generally track the major fiber bundles. This suggests that only a few voxels covering the cross-sectional area of the major fiber bundles are needed for consistent tractography as long as we can reconstruct the complex fiber configurations as seen in the higher resolutions (Dyrby et al., 2014). The SNR is the key parameter for robust disentangling of the voxel-wise complex (multi) fiber configurations (Froeling et al., 2016). At lower image resolution we get higher SNR which makes it possible to reconstruct the detailed fiber configurations as

seen in the higher image resolution. In agreement with our results, when SNR is limited, the higher image resolution is not guaranteed to reconstruct much finer detailed fiber configurations than the low image resolution with a high SNR. Interestingly, this suggests that when mapping a structural connectome, one should use an image resolution that allows detection of the major fiber bundles which also ensures a high SNR, while prioritizing high angular resolution data acquisition. However, there may exist a yet unknown relation between image resolution, size of fiber bundles, and the size of the tracer graph. Larger fiber bundles can intermingle in a dense parallel funnel, i.e., a bottleneck region through which their true projection can be a challenge to follow (Maier-Hein et al., 2017; Sarubbo et al., 2019). Similarly, we demonstrated that lowering the image resolution increases the risk of severe partial volume effects (PVE) where new connections (false positives) also can appear by tractography “jumping” between neighbouring connections. For example, the incision in the left occipital cortex physically separated occipital connections in visual cortex. These connections are clearly disrupted when tracking in high image resolution, but not in low image resolution. However, when comparing the intact hemisphere with the one with the incision, only minor differences are seen in sensitivity and specificity (results not shown). The reason could be that sensitivity and specificity do not take the strength of the connections into account, but only use the binary information whether a connection is present or absent. Hence, if just a few streamlines cross the incision, the regions are still considered connected at low thresholds. In contrast, cross entropy uses the weights of the connections and these results show that the intact hemisphere outperforms the hemisphere with the incision.

The sufficient image resolution for tractography and SC is an open question, but appears to be related to its cross-sectional size and organisation. The image resolution, obtainable with MRI, may not easily solve the complexity of fiber organisation (Schilling et al., 2017), so the actual question is how larger axonal bundles are organised, into which tracers provide insights (Schmahmann and Pandya, 2009).

4.2. Limitations of the tracer graph

The effective image resolution of tractography may also be closely linked to the size of the tracer graph. The analyses performed in the present study may be challenged by the coarse resolution of the M132 parcellation. The substantial subsampling of the tractography graph may limit the amount of information we can extract from the diffusion data, complicating appropriate comparison of different settings. Furthermore, the coarse resolution of the M132 parcellation can potentially be a factor favouring graphs derived from low resolution images over those derived from the high image resolution. This limitation may be overcome by an even more comprehensive tracer graph than the one provided by Markov et al., 2014. However, the tracer graph by Markov et al. is the most detailed tracer connectivity study in monkeys currently available. As discussed in Knösche et al. (2015), invasive tracers have their own challenges, such that not all neurons are labeled within an injected brain region, making the tracer more of a “silver” than a gold standard (see also (Dyrby et al., 2018) for a review). Another limitation of the tracer graph is that it is only available for intra-hemispheric connections. Hence, long-range inter-hemispheric connections also known to be challenging to track are not considered in the analysis. Thus, the performance metrics may represent an upper bound for whole-brain connectome reconstruction. Furthermore, the tractography graph is symmetric by construction whereas the tracer graph is asymmetric.

4.3. The impact of step length, seeding strategy and streamline count threshold

We find that the integration step length in the tractography influence the result and that larger step lengths improve the results. This is in agreement with Dauguet et al. (2007) and Tournier et al. (2012) who recommend using the largest step length that provides sufficient

accuracy. However, a tractography parameter not explored herein is the maximum turning angle. When adjusting the step size in the tractography, the maximum turning angle is not changed. This means that when the step size is decreased, the streamlines can make much sharper turns. This could have an impact on the results for different step sizes (Fig. 6). Furthermore, we find that the seeding strategy has a minimal impact on the graph performance which is in agreement with some previous findings (Donahue et al., 2016), but in contradiction to others (Buchanan et al., 2014). Li et al. have found that when using WM seeding, the graphs are biased towards long fiber tracts, because larger tracts contain more seed voxels than short pathways, whereas GM tractography is biased towards short pathways (Li et al., 2011). Thus, the SC graphs are sparser when using GM seeding compared to WM seeding. This implies, that lower streamline count thresholds are needed to ensure a balanced compromise between sensitivity and specificity when performing GM seeding compared to WM seeding (WM seeding: Fig. 7, GM seeding: results not shown). Despite this, we observed a sustained balanced compromise between sensitivity and specificity at 60–64% in agreement with other studies that uses the same tracer material and analyses (Donahue et al., 2016). However, our results show that the streamline count threshold ensuring a balanced compromise between sensitivity and specificity depends on the data acquisition parameters, except for the combination of the lowest angular resolution and the highest b-value. Here, a high b-value provides finer angular information, which cannot be captured with low angular resolution and compensated by a higher SNR.

4.4. Performance metrics

Other studies validating brain networks used various performance metrics when comparing tracer and tractography graphs using e.g. accuracy (percentage of correctly determined binary connections) (Azadbakht et al., 2015), correlation between FLNe and FSe (fraction of streamlines connecting two areas relative to the number of streamlines extrinsic to those areas) (Donahue et al., 2016) or correlation between number of streamlines and FLNe (van den Heuvel et al., 2015). As performance metrics, we used cross entropy and ROC, and found large differences in the results. The cross entropy was applied between FLNe (fraction of labeled counted neurons extrinsic to the target region) distribution and the connectivity distribution quantified from streamline tractography by Bayesian inference. Cross entropy uses all the information (weights) available in the graphs, i.e. no need for thresholding. The cross entropy results show that thresholding the tractography graph has minimal effect on the overall cross entropy result, i.e. the ranking of the graphs. The ROC analysis that is a widely used performance metric, compares binarized graphs by thresholding both the tracer and the tractography graph. Surprisingly, the ROC results did not show dependence on any scanning parameters when thresholding the tracer graph by whether a connection exists or not (i.e. FLNe > 0). Only by increasing the tracer graph threshold the balance between sensitivity and specificity increased. Hence, our results suggest that important information in SC analyses risks to be lost if using performance metrics based on binarization of the tracer graph that is assumed to be the gold standard.

4.5. Considerations

In the cortical termination of a streamline, partial volume effects influence the point of termination and this may be improved by correcting the SC graphs for gyral crown biases (Van Essen et al., 2014) as done in Donahue et al. (2016). In addition, path-length dependencies (PLD) are introduced in probabilistic tractography, and hence unwanted loss of streamline counts for longer tracts can have an impact on SC (Liptrot et al., 2014). In Donahue et al. (2016), we demonstrated reduced PLD effects in SC analysis by using an exponential fit. Here, we validated the impact of varying the acquisition parameters, and we found a sensitivity/specificity trade-off approximately 5% lower than reported in Donahue et al. (2016). This suggests that correcting the above-mentioned

tractography bias improve the SC graph, independent upon the performance metric used. Algorithms, besides from exploring image resolution, could include topological (Innocenti et al., 2019; Sarubbo et al., 2019) and multimodal microstructure informed tracking (Daducci et al., 2016).

Indeed, we only applied the FSL tractography method, but to our knowledge, no generally used tractography method that outperform all others exist (Knösche et al., 2015; Maier-Hein et al., 2017; Schilling et al., 2019). Therefore, our results are believed to be generally representative to the challenges of the research field, including in vivo human as *ex vivo* dMRI is translational to human. Finally, we applied the comprehensive acquisition parameter space to a single *ex vivo* monkey brain only. However, since we investigated differences between different acquisition parameters within a subject, more subjects are expected to lead to the same overall conclusions, assuming that subjects have similar anatomy. This is also supported by the findings by Donahue et al. (2016), who get similar results in different monkeys.

5. Conclusion

The cross entropy was used as a similarity measure to evaluate how scanning parameters impact the SC analysis. Lower image resolution can improve the agreement between SC graphs from postmortem monkey brains and a tracer graph mapped onto the M132 cortical parcellation. This suggests that SC is dominated by major tracts that also are present at the lower image resolution which also benefits of a higher SNR. However, since the tracer data only provides a spatial distribution of labeled neurons in cortical source and target regions and not the axonal trajectories, we cannot verify the geometrical shapes i.e. sizes of labeled tracts. Similarly, we find that high angular resolution and high SNR compared to b-value are important parameters for SC. Interestingly, independent of the different scanner parameter settings, the balanced compromise between sensitivity and specificity remains constant around 60–64% but appears as a lower bound dependent upon the selected tracer graph threshold. Hence, using performance metrics like the ROC curves that are based on thresholded graphs one may risk to loose information in the comparison of tractography and tracer data. Finally, we ensured that the scanning parameters applied to the *ex vivo* monkey brain are translational to an in vivo human brain in terms of image resolution, b-value, and angular resolution. We therefore expect that our findings are translational.

Acknowledgement

We wish to thank Thomas Knösche, MPI in Leipzig for good discussions in relation to SNR and image resolution. This project was supported by the Lundbeck Foundation, fellowship grant no. R105-9813 to Morten Mørup.

Appendix A. Supplementary data

Supplementary data to this article can be found online at <https://doi.org/10.1016/j.neuroimage.2019.116207>.

References

- Ahmed, B., Corderly, P.M., McLelland, D., Bair, W., Krug, K., 2012. Long-range clustered connections within extrastriate visual area V5/MT of the rhesus macaque. *Cerebr. Cortex* 22, 60–73.
- Ambrosen, K.S., Albers, K.J., Dyrby, T.B., Schmidt, M.N., Mørup, M., 2014. Nonparametric Bayesian clustering of structural whole brain connectivity in full image resolution. In: 2014 International Workshop on Pattern Recognition in Neuroimaging. <https://doi.org/10.1109/prni.2014.6858507>.
- Anwander, A., Tittgemeyer, M., von Cramon, D.Y., Friederici, A.D., Knösche, T.R., 2007. Connectivity-based parcellation of broca's area. *Cerebr. Cortex* 17, 816–825.
- Avants, B.B., Epstein, C.L., Grossman, M., Gee, J.C., 2008. Symmetric diffeomorphic image registration with cross-correlation: evaluating automated labeling of elderly and neurodegenerative brain. *Med. Image Anal.* 12, 26–41.
- Azadbakht, H., Parkes, L.M., Haroon, H.A., Augath, M., Logothetis, N.K., de Crespigny, A., D'Arceuil, H.E., Parker, G.J.M., 2015. Validation of high-resolution tractography against in vivo tracing in the macaque visual cortex. *Cerebr. Cortex* 25, 4299–4309.

- Baldassano, C., Beck, D.M., Fei-Fei, L., 2015. Parcellating connectivity in spatial maps. *PeerJ* 3, e784.
- Basser, P.J., Mattiello, J., LeBihan, D., 1994. MR diffusion tensor spectroscopy and imaging. *Biophys. J.* 66, 259–267.
- Bastiani, M., Shah, N.J., Goebel, R., Roebroeck, A., 2012. Human cortical connectome reconstruction from diffusion weighted MRI: the effect of tractography algorithm. *Neuroimage* 62, 1732–1749.
- Behrens, T.E.J., Berg, H.J., Jbabdi, S., Rushworth, M.F.S., Woolrich, M.W., 2007. Probabilistic diffusion tractography with multiple fibre orientations: what can we gain? *Neuroimage* 34, 144–155.
- Behrens, T.E.J., Johansen-Berg, H., Woolrich, M.W., Smith, S.M., Wheeler-Kingshott, C.A.M., Boulby, P.A., Barker, G.J., Sillery, E.L., Sheehan, K., Ciccarelli, O., Thompson, A.J., Brady, J.M., Matthews, P.M., 2003a. Non-invasive mapping of connections between human thalamus and cortex using diffusion imaging. *Nat. Neurosci.* 6, 750–757.
- Behrens, T.E.J., Woolrich, M.W., Jenkinson, M., Johansen-Berg, H., Nunes, R.G., Clare, S., Matthews, P.M., Brady, J.M., Smith, S.M., 2003b. Characterization and propagation of uncertainty in diffusion-weighted MR imaging. *Magn. Reson. Med.* 50, 1077–1088.
- Bennett, L.J., Madden, D.J., Vaidya, C.J., Howard, D.V., Howard Jr., J.H., 2010. Age-related differences in multiple measures of white matter integrity: a diffusion tensor imaging study of healthy aging. *Hum. Brain Mapp.* 31, 378–390.
- Berman, J.I., Lanza, M.R., Blaskey, L., Edgar, J.C., Roberts, T.P.L., 2013. High angular resolution diffusion imaging probabilistic tractography of the auditory radiation. *AJNR Am. J. Neuroradiol.* 34, 1573–1578.
- Buchanan, C.R., Pernet, C.R., Gorgolewski, K.J., Storkey, A.J., Bastin, M.E., 2014. -. *Neuroimage* 86, 231–243.
- Caiafa, C.F., Pestilli, F., 2017. Multidimensional encoding of brain connectomes. *Sci. Rep.* 7, 11491.
- Calabrese, E., Badaea, A., Cofer, G., Qi, Y., Johnson, G.A., 2015. A diffusion MRI tractography connectome of the mouse brain and comparison with neuronal tracer data. *Cerebr. Cortex* 25, 4628–4637.
- Chen, L., Wagenknecht, G., 2006. Automated topology correction for human brain segmentation. *Med. Image Comput. Comput. Assist. Interv.* 9, 316–323.
- Coupe, P., Yger, P., Prima, S., Hellier, P., Kervrann, C., Barillot, C., 2008. An optimized blockwise nonlocal means denoising filter for 3-D magnetic resonance images. *IEEE Trans. Med. Imaging* 27, 425–441.
- Craddock, R.C., Jbabdi, S., Yan, C.-G., Vogelstein, J.T., Castellanos, F.X., Di Martino, A., Kelly, C., Heberlein, K., Colcombe, S., Milham, M.P., 2013. Imaging human connectomes at the macroscale. *Nat. Methods* 10, 524–539.
- Daducci, A., Dal Palú, A., Descoteaux, M., Thiran, J.-P., 2016. Microstructure informed tractography: pitfalls and open challenges. *Front. Neurosci.* 10, 247.
- D'Arceuil, H.E., Westmoreland, S., de Crespigny, A.J., 2007. An approach to high resolution diffusion tensor imaging in fixed primate brain. *Neuroimage* 35, 553–565.
- Dauguet, J., Peled, S., Berezovskii, V., Delzescaux, T., Warfield, S.K., Born, R., Westin, C.-F., 2007. Comparison of fiber tracts derived from in-vivo DTI tractography with 3D histological neural tract reconstruction on a macaque brain. *Neuroimage* 37, 530–538.
- de Reus, M.A., van den Heuvel, M.P., 2013. Estimating false positives and negatives in brain networks. *Neuroimage* 70, 402–409.
- Donahue, C.J., Sotiropoulos, S.N., Jbabdi, S., Hernandez-Fernandez, M., Behrens, T.E., Dyrby, T.B., Coalson, T., Kennedy, H., Knoblauch, K., Van Essen, D.C., Glasser, M.F., 2016. Using diffusion tractography to predict cortical connection strength and distance: a quantitative comparison with tracers in the monkey. *J. Neurosci.* 36, 6758–6770.
- Dyrby, T.B., Baaré, W.F.C., Alexander, D.C., Jelsing, J., Garde, E., Søgaard, L.V., 2011. An ex vivo imaging pipeline for producing high-quality and high-resolution diffusion-weighted imaging datasets. *Hum. Brain Mapp.* 32, 544–563.
- Dyrby, T.B., Innocenti, G.M., Bech, M., Lundell, H., 2018. Validation strategies for the interpretation of microstructure imaging using diffusion MRI. *Neuroimage* 182, 62–79. <https://doi.org/10.1016/j.neuroimage.2018.06.049>.
- Dyrby, T.B., Lundell, H., Burke, M.W., Reisle, N.L., Paulson, O.B., Pfitz, M., Siebner, H.R., 2014. Interpolation of diffusion weighted imaging datasets. *Neuroimage* 103, 202–213.
- Dyrby, T.B., Søgaard, L.V., Parker, G.J., Alexander, D.C., Lind, N.M., Baaré, W.F.C., Hay-Schmidt, A., Eriksen, N., Pakkenberg, B., Paulson, O.B., Jelsing, J., 2007. Validation of in vitro probabilistic tractography. *Neuroimage* 37, 1267–1277.
- Eskildsen, S.F., Østergaard, L.R., 2008. Evaluation of five algorithms for mapping brain cortical surfaces. In: 2008 XXI Brazilian Symposium on Computer Graphics and Image Processing. <https://doi.org/10.1109/sibgrapi.2008.16>.
- Eskildsen, S.F., Østergaard, L.R., 2007. Quantitative comparison of two cortical surface extraction methods using MRI phantoms. *Med. Image Comput. Comput. Assist. Interv.* 10, 409–416.
- Eskildsen, S.F., Østergaard, L.R., 2006. Active surface approach for extraction of the human cerebral cortex from MRI. *Med. Image Comput. Comput. Assist. Interv.* 9, 823–830.
- Eskildsen, S.F., Uldahl, M., Østergaard, L.R., 2005. Extraction of the cerebral cortical boundaries from MRI for measurement of cortical thickness. In: *Medical Imaging 2005: Image Processing*. <https://doi.org/10.1117/12.595145>.
- Fan, L., Li, H., Zhuo, J., Zhang, Y., Wang, J., Chen, L., Yang, Z., Chu, C., Xie, S., Laird, A.R., Fox, P.T., Eickhoff, S.B., Yu, C., Jiang, T., 2016. The human brainnetome atlas: a new brain atlas based on connective architecture. *Cerebr. Cortex* 26, 3508–3526.
- Fornito, A., Zalesky, A., Breakspear, M., 2013. Graph analysis of the human connectome: promise, progress, and pitfalls. *Neuroimage* 80, 426–444.
- Frank, L.R., 2002. Characterization of anisotropy in high angular resolution diffusion-weighted MRI. *Magn. Reson. Med.* 47, 1083–1099.
- Frank, L.R., 2001. Anisotropy in high angular resolution diffusion-weighted MRI. *Magn. Reson. Med.* 45, 935–939.
- Froeling, M., Tax, C.M.W., Vos, S.B., Luijten, P.R., Leemans, A., 2016. “MASSIVE” brain dataset: multiple acquisitions for standardization of structural imaging validation and evaluation. *Magn. Reson. Med.* 77 (5), 1797–1809. <https://doi.org/10.1002/mrm.26259>.
- Gigandet, X., Griffa, A., Kober, T., Daducci, A., Gilbert, G., Connelly, A., Hagmann, P., Meuli, R., Thiran, J.-P., Krueger, G., 2013. A connectome-based comparison of diffusion MRI schemes. *PLoS One* 8, e75061.
- Giorgio, A., Palace, J., Johansen-Berg, H., Smith, S.M., Ropele, S., Fuchs, S., Wallner-Blazek, M., Enzinger, C., Fazekas, F., 2010. Relationships of brain white matter microstructure with clinical and MR measures in relapsing-remitting multiple sclerosis. *J. Magn. Reson. Imaging* 31, 309–316.
- Gong, G., Rosa-Neto, P., Carbonell, F., Chen, Z.J., He, Y., Evans, A.C., 2009. Age- and gender-related differences in the cortical anatomical network. *J. Neurosci.* 29, 15684–15693.
- Gudbjartsson, H., Patz, S., 1995. The Rician distribution of noisy MRI data. *Magn. Reson. Med.* 34, 910–914.
- Hagmann, P., 2005. From Diffusion MRI to Brain Connectomics. Institut de traitement de signaux PROGRAMME DOCTORAL EN INFORMATIQUE ET COMMUNICATIONS POUR L'OBTENTION DU GRADE DE DOCTEUR ÈS SCIENCES PAR Docteur en médecine, Université de Lausanne.
- Hinne, M., Janssen, R.J., Heskens, T., van Gerven, M.A.J., 2015. Bayesian estimation of conditional independence graphs improves functional connectivity estimates. *PLoS Comput. Biol.* 11, e1004534.
- Innocenti, G.M., Dyrby, T.B., Girard, G., St-Onge, E., Thiran, J.-P., Daducci, A., Descoteaux, M., 2019. Topological principles and developmental algorithms might refine diffusion tractography. *Brain Struct. Funct.* 224, 1–8.
- Iturria-Medina, Y., 2013. Anatomical brain networks on the prediction of abnormal brain states. *Brain Connect.* 3, 1–21.
- Jahanshad, N., Nir, T.M., Toga, A.W., Jack Jr., C.R., Bernstein, M.A., Weiner, M.W., Thompson, P.M., 2015. Alzheimer's Disease Neuroimaging Initiative, 2015. Seemingly unrelated regression empowers detection of network failure in dementia. *Neurobiol. Aging* 36 (Suppl. 1), S103–S112. <https://www.ncbi.nlm.nih.gov/pubmed/25257986>.
- Jbabdi, S., Lehman, J.F., Haber, S.N., Behrens, T.E., 2013. Human and monkey ventral prefrontal fibers use the same organizational principles to reach their targets: tracing versus tractography. *J. Neurosci.* 33, 3190–3201.
- Jenkinson, M., Beckmann, C.F., Behrens, T.E.J., Woolrich, M.W., Smith, S.M., 2012. FSL. *Neuroimage* 62, 782–790.
- Jones, D.K., 2004. The effect of gradient sampling schemes on measures derived from diffusion tensor MRI: a Monte Carlo study. *Magn. Reson. Med.* 51, 807–815.
- Jones, D.K., Cercignani, M., 2010. Twenty-five pitfalls in the analysis of diffusion MRI data. *NMR Biomed.* 23, 803–820.
- Jones, D.K., Knösche, T.R., Turner, R., 2013. White matter integrity, fiber count, and other fallacies: the do's and don'ts of diffusion MRI. *Neuroimage* 73, 239–254.
- Knösche, T.R., Anwender, A., Liptrot, M., Dyrby, T.B., 2015. Validation of tractography: comparison with manganese tracing. *Hum. Brain Mapp.* 36, 4116–4134.
- Kullback, S., Leibler, R.A., 1951. On information and sufficiency. *Ann. Math. Stat.* 22, 79–86.
- Lebel, C., Walker, L., Leemans, A., Phillips, L., Beaulieu, C., 2008. Microstructural maturation of the human brain from childhood to adulthood. *Neuroimage* 40, 1044–1055.
- Le Bihan, D., Johansen-Berg, H., 2012. Diffusion MRI at 25: exploring brain tissue structure and function. *Neuroimage* 61, 324–341.
- Li, L., Rilling, J.K., Preuss, T.M., Glasser, M.F., Hu, X., 2011. The effects of connection reconstruction method on the interregional connectivity of brain networks via diffusion tractography. *Hum. Brain Mapp.* 33, 1894–1913.
- Liptrot, M.G., Sidaros, K., Dyrby, T.B., 2014. Addressing the path-length-dependency confound in white matter tract segmentation. *PLoS One* 9, e96247.
- Lo, C.-Y., Wang, P.-N., Chou, K.-H., Wang, J., He, Y., Lin, C.-P., 2010. Diffusion tensor tractography reveals abnormal topological organization in structural cortical networks in Alzheimer's disease. *J. Neurosci.* 30, 16876–16885.
- Lorensen, W.E., Cline, H.E., 1987. Marching cubes: a high resolution 3D surface construction algorithm. *ACM SIGGRAPH Comput. Graph.* 21, 163–169.
- Maier-Hein, K.H., Neher, P.F., Houde, J.-C., Côté, M.-A., Garyfallidis, E., Zhong, J., Chamberland, M., Yeh, F.-C., Lin, Y.-C., Ji, Q., Reddick, W.E., Glass, J.O., Chen, D.Q., Feng, Y., Gao, C., Wu, Y., Ma, J., Renjie, H., Li, Q., Westin, C.-F., Deslauriers-Gauthier, S., González, J.O.O., Paquette, M., St-Jean, S., Girard, G., Rheault, F., Sidhu, J., Tax, C.M.W., Guo, F., Mesri, H.Y., Dávid, S., Froeling, M., Heemskerck, A.M., Leemans, A., Boré, A., Pinsard, B., Bedetti, C., Desrosiers, M., Brambati, S., Doyon, J., Sarica, A., Vasta, R., Cerasa, A., Quattrone, A., Yeatman, J., Khan, A.R., Hodges, W., Alexander, S., Romascano, D., Barakovic, M., Auria, A., Esteban, O., Lemkaddem, A., Thiran, J.-P., Cetingul, H.E., Odry, B.L., Mailhe, B., Nadar, M.S., Pizzagalli, F., Prasad, G., Villalón-Reina, J.E., Galvis, J., Thompson, P.M., Requijo, F.D.S., Laguna, P.L., Lacerda, L.M., Barrett, R., Dell'Acqua, F., Catani, M., Petit, L., Caruyer, E., Daducci, A., Dyrby, T.B., Holland-Letz, T., Hilgetag, C.C., Stieltjes, B., Descoteaux, M., 2017. The challenge of mapping the human connectome based on diffusion tractography. *Nat. Commun.* 8, 1349.
- Markov, N.T., Ersey-Ravasz, M.M., Ribeiro Gomes, A.R., Lamy, C., Magrou, L., Vezoli, J., Misery, P., Falchier, A., Quilodran, R., Gariel, M.A., Sallet, J., Gamanut, R., Huissoud, C., Clavagnier, S., Giroud, P., Sappey-Marinière, D., Barone, P., Dehay, C., Toroczkai, Z., Knoblauch, K., Van Essen, D.C., Kennedy, H., 2014. A weighted and directed interareal connectivity matrix for macaque cerebral cortex. *Cerebr. Cortex* 24, 17–36.

- Markov, N.T., Misery, P., Falchier, A., Lamy, C., Vezoli, J., Quilodran, R., Gariel, M.A., Giroud, P., Ercsey-Ravasz, M., Pilaz, L.J., Huissoud, C., Barone, P., Dehay, C., Toroczkai, Z., Van Essen, D.C., Kennedy, H., Knoblauch, K., 2011. Weight consistency specifies regularities of macaque cortical networks. *Cerebr. Cortex* 21, 1254–1272.
- Parisot, S., Arslan, S., Passerat-Palmbach, J., Wells 3rd, W.M., Rueckert, D., 2016. Group-wise parcellation of the cortex through multi-scale spectral clustering. *Neuroimage* 136, 68–83.
- Pestilli, F., Yeatman, J.D., Rokem, A., Kay, K.N., Wandell, B.A., 2014. Evaluation and statistical inference for human connectomes. *Nat. Methods* 11, 1058–1063.
- Pierpaoli, C., Jezzard, P., Basser, P.J., Barnett, A., Di Chiro, G., 1996. Diffusion tensor MR imaging of the human brain. *Radiology* 201, 637–648.
- Qi, S., Meesters, S., Nicolay, K., ter Haar Romeny, B.M., Ossenblok, P., 2015. The influence of construction methodology on structural brain network measures: a review. *J. Neurosci. Methods* 253, 170–182.
- Robinson, E.C., Hammers, A., Ericsson, A., David Edwards, A., Rueckert, D., 2010. Identifying population differences in whole-brain structural networks: a machine learning approach. *Neuroimage* 50, 910–919.
- Sarubbo, S., Petit, L., De Benedictis, A., Chioffi, F., Pfito, M., Dyrby, T.B., 2019. Uncovering the inferior fronto-occipital fascicle and its topological organization in non-human primates: the missing connection for language evolution. *Brain Struct. Funct.* 224 (4), 1553–1567. <https://doi.org/10.1007/s00429-019-01856-2>.
- Schilling, K., Gao, Y., Janve, V., Stepniewska, I., Landman, B.A., Anderson, A.W., 2017. Can increased spatial resolution solve the crossing fiber problem for diffusion MRI? *NMR Biomed.* 30. <https://doi.org/10.1002/nbm.3787>.
- Schilling, K.G., Nath, V., Hansen, C., Parvathaneni, P., Blaber, J., Gao, Y., Neher, P., Aydogan, D.B., Shi, Y., Ocampo-Pineda, M., Schiavi, S., Daducci, A., Girard, G., Barakovic, M., Rafael-Patino, J., Romascano, D., Rensonnet, G., Pizzolato, M., Bates, A., Fische, E., Thiran, J.-P., Canales-Rodriguez, E.J., Huang, C., Zhu, H., Zhong, L., Cabeen, R., Toga, A.W., Rheault, F., Theaud, G., Houde, J.-C., Sidhu, J., Chamberland, M., Westin, C.-F., Dyrby, T.B., Verma, R., Rathi, Y., Irfanoglu, M.O., Thomas, C., Pierpaoli, C., Descoteaux, M., Anderson, A.W., Landman, B.A., 2019. Limits to anatomical accuracy of diffusion tractography using modern approaches. *Neuroimage* 185, 1–11.
- Schmahmann, J., Pandya, D., 2009. *Fiber Pathways of the Brain*. Oxford University Press, USA.
- Shannon, C.E., 1948. A mathematical theory of communication. *Bell Syst. Tech. J.* 27, 623–656.
- Shu, N., Liu, Y., Li, K., Duan, Y., Wang, J., Yu, C., Dong, H., Ye, J., He, Y., 2011. Diffusion tensor tractography reveals disrupted topological efficiency in white matter structural networks in multiple sclerosis. *Cerebr. Cortex* 21, 2565–2577.
- Skudlarski, P., Jagannathan, K., Anderson, K., Stevens, M.C., Calhoun, V.D., Skudlarska, B.A., Pearlson, G., 2010. Brain connectivity is not only lower but different in schizophrenia: a combined anatomical and functional approach. *Biol. Psychiatry* 68, 61–69.
- Sled, J.G., Zijdenbos, A.P., Evans, A.C., 1998. A nonparametric method for automatic correction of intensity nonuniformity in mri data. *IEEE Trans. Med. Imaging* 17 (1), 87–97.
- Smith, S.M., Jenkinson, M., Woolrich, M.W., Beckmann, C.F., Behrens, T.E.J., Johansen-Berg, H., Bannister, P.R., De Luca, M., Drobnjak, I., Flitney, D.E., Niazy, R.K., Saunders, J., Vickers, J., Zhang, Y., De Stefano, N., Brady, J.M., Matthews, P.M., 2004. Advances in functional and structural MR image analysis and implementation as FSL. *Neuroimage* 23 (Suppl. 1), S208–S219.
- Sotiropoulos, S.N., Jbabdi, S., Xu, J., Andersson, J.L., Moeller, S., Auerbach, E.J., Glasser, M.F., Hernandez, M., Sapiro, G., Jenkinson, M., Feinberg, D.A., Yacoub, E., Lenglet, C., Van Essen, D.C., Ugurbil, K., Behrens, T.E.J., WU-Minn HCP Consortium, 2013. Advances in diffusion MRI acquisition and processing in the human connectome project. *Neuroimage* 80, 125–143.
- Sporns, O., Tononi, G., Kötter, R., 2005. The human connectome: a structural description of the human brain. *PLoS Comput. Biol.* 1, e42.
- Sun, S.-W., Neil, J.J., Liang, H.-F., He, Y.Y., Schmidt, R.E., Hsu, C.Y., Song, S.-K., 2005. Formalin fixation alters water diffusion coefficient magnitude but not anisotropy in infarcted brain. *Magn. Reson. Med.* 53, 1447–1451.
- Thomas, C., Ye, F.Q., Irfanoglu, M.O., Modi, P., Saleem, K.S., Leopold, D.A., Pierpaoli, C., 2014. Anatomical accuracy of brain connections derived from diffusion MRI tractography is inherently limited. *Proc. Natl. Acad. Sci. U.S.A.* 111, 16574–16579.
- Toga, A.W., Thompson, P.M., Mori, S., Amunts, K., Zilles, K., 2006. Towards multimodal atlases of the human brain. *Nat. Rev. Neurosci.* 7, 952–966.
- Tournier, J.-D., Calamante, F., Connelly, A., 2012. MRtrix: diffusion tractography in crossing fiber regions. *Int. J. Imaging Syst. Technol.* 22, 53–66.
- van den Heuvel, M.P., de Reus, M.A., Feldman Barrett, L., Scholtens, L.H., Coopmans, F.M.T., Schmidt, R., Preuss, T.M., Rilling, J.K., Li, L., 2015. Comparison of diffusion tractography and tract-tracing measures of connectivity strength in rhesus macaque connectome. *Hum. Brain Mapp.* 36, 3064–3075.
- Van Essen, D.C., 2002. Surface-based atlases of cerebellar cortex in the human, macaque, and mouse. *Ann. N. Y. Acad. Sci.* 978, 468–479.
- Van Essen, D.C., Dierker, D.L., 2007. Surface-based and probabilistic atlases of primate cerebral cortex. *Neuron* 56, 209–225.
- Van Essen, D.C., Jbabdi, S., Sotiropoulos, S.N., Chen, C., Dikranian, K., Coalson, T., Harwell, J., Behrens, T.E.J., Glasser, M.F., 2014. Mapping connections in humans and non-human primates. In: *Diffusion MRI*, pp. 337–358.
- Villalon-Reina, J.E., Nir, T.M., Zhan, L., McMahon, K.L., de Zubicaray, G.I., Wright, M.J., Jahanshad, N., Thompson, P.M., 2016. Reliability of structural connectivity examined with four different diffusion reconstruction methods at two different spatial and angular resolutions. In: *Mathematics and Visualization*, pp. 219–231.
- Vos, S.B., Aksoy, M., Han, Z., Holdsworth, S.J., Maclaren, J., Viergever, M.A., Leemans, A., Bammer, R., 2016. Trade-off between angular and spatial resolutions in vivo fiber tractography. *Neuroimage* 129, 117–132.
- Wen, W., Zhu, W., He, Y., Kochan, N.A., Reppermund, S., Slavin, M.J., Brodaty, H., Crawford, J., Xia, A., Sachdev, P., 2011. Discrete neuroanatomical networks are associated with specific cognitive abilities in old age. *J. Neurosci.* 31, 1204–1212.
- Wiegell, M.R., Tuch, D.S., Larsson, H.B.W., Wedeen, V.J., 2003. Automatic segmentation of thalamic nuclei from diffusion tensor magnetic resonance imaging. *Neuroimage* 19, 391–401.
- Woolrich, M.W., Jbabdi, S., Patenaude, B., Chappell, M., Makni, S., Behrens, T., Beckmann, C., Jenkinson, M., Smith, S.M., 2009. Bayesian analysis of neuroimaging data in FSL. *Neuroimage* 45, S173–S186.
- Xie, S., Zuo, N., Shang, L., Song, M., Fan, L., Jiang, T., 2015. How does B-value affect HARDI reconstruction using clinical diffusion MRI data? *PLoS One* 10, e0120773.
- Zalesky, A., Cocchi, L., Fornito, A., Murray, M.M., Bullmore, E., 2012. Connectivity differences in brain networks. *Neuroimage* 60, 1055–1062.
- Zalesky, A., Fornito, A., Bullmore, E.T., 2010. Network-based statistic: identifying differences in brain networks. *Neuroimage* 53, 1197–1207.
- Zalesky, A., Fornito, A., Seal, M.L., Cocchi, L., Westin, C.-F., Bullmore, E.T., Egan, G.F., Pantelis, C., 2011. Disrupted axonal fiber connectivity in schizophrenia. *Biol. Psychiatry* 69, 80–89.
- Zhang, Y., Brady, M., Smith, S., 2001. Segmentation of brain MR images through a hidden Markov random field model and the expectation-maximization algorithm. *IEEE Trans. Med. Imaging* 20, 45–57.
- Zhan, L., Franc, D., Patel, V., Jahanshad, N., Jin, Y., Mueller, B.A., Bernstein, M.A., Borowski, B.J., Jack Jr., C.R., Toga, A.W., Lim, K.O., Thompson, P.M., 2012. HOW do spatial and angular resolution affect brain connectivity maps from diffusion MRI? *Proc. IEEE Int. Symp. Biomed. Imag.* 1–6.
- Zhan, L., Leow, A.D., Jahanshad, N., Chiang, M.-C., Barysheva, M., Lee, A.D., Toga, A.W., McMahon, K.L., de Zubicaray, G.I., Wright, M.J., Thompson, P.M., 2010. How does angular resolution affect diffusion imaging measures? *Neuroimage* 49, 1357–1371.